High-Entropy Ti, Zr, Hf, Ta Multiphase Diboride with Deformation Resistance up to 2000 °C

[1,*]Petre Badica, [1]Mihai Alexandru Grigoroscuta, [1]Andrei Kuncser, [2,*]Oleg Vasylkiv

[1]National Institute of Materials Physics, Atomistilor street 405A, 077125 Magurele, Romania
[2]National Institute for Materials Science, 1-2-1 Sengen, Tsukuba, Ibaraki 305-0047, Japan

*Corresponding authors:
O. Vasylkiv oleg.vasylkiv@nims.go.jp
P. Badica: badica2003@yahoo.com, petre.badica@infim.ro

Submitted to ***Advanced Engineering Materials***

High-Entropy Ti, Zr, Hf, Ta Multiphase Diboride with Deformation Resistance up to 2000 °C

[1*]P. Badica, [1]M.A. Grigoroscuta, [1]A. Kuncser, [2,*]O. Vasylkiv

[1]National Institute of Materials Physics, Atomistilor street 405A, 077125 Magurele, Romania
[2]National Institute for Materials Science, 1-2-1 Sengen, Tsukuba, Ibaraki 305-0047, Japan

*Corresponding authors:
O. Vasylkiv oleg.vasylkiv@nims.go.jp
P. Badica: badica2003@yahoo.com, petre.badica@infim.ro

Abstract

A multiphase high entropy diboride $(Ti_{0.25}Ta_{0.25}Hf_{0.25}Zr_{0.25})B_2$ was obtained by spark plasma sintering from a mixture of single-metal diborides. The as-prepared material at the microscale can be defined as a composite where grains of a Ta-rich/Ti-poor complex diboride phase are the reinforcement and grains of Ta-poor/Ti-rich complex diboride are the matrix. However, at the nanoscale, the grains are heterogeneous, composed of regions with a multitude of complex diboride compositions. The interface between nano regions is compositionally graded and has an irregular shape. The four-metal diboride shows a deformation-resistant mechanism under bending load. A strengthening process is active, increasing the room temperature bending strength (326 MPa) by ~50 % at 1800 °C (488 MPa). A ductile behavior with a deformation strain of ~7.5 % is observed at 2000 °C while bending strength (407 MPa) is ~25 % above the value at room temperature. At 2000 °C, observation of dislocations propagating from one compositional nano region to another and with a different density suggests dislocation contribution, first of all, to plasticity. The peculiar heterogeneity of this material at nano and micro scales is considered the reason for the remarkable mechanical response to bending load at different temperatures.

Keywords: high entropy diboride; high temperature bending test; microstructure; plasticity; spark plasma sintering.

1. Introduction

Performance enhancement of existing applications and fabrication of new ones require searching, designing, and obtaining of new materials. Applications from energy and aerospace industries working in extreme conditions need special materials with capabilities beyond those of the available ones. *High entropy materials* (HEM) were proposed as a new class to respond to the challenges. The first studied HEMs were high entropy alloys [1, 2] with equimolar proportions of the component metals. The concept of obtaining single-phase solid solutions between four, usually five, or more metals, mostly with similar crystal structures, proved rewarding, and they have shown excellent properties exceeding typical alloys built around a dominant metal alloyed in small concentrations by other elements. Sometimes, ternary solid solutions are labeled as *m*edium *e*ntropy *m*aterials (MEM) [3, 4]. The concept was extended to other compounds such as oxides, carbides, borides, nitrides, silicides, fluorides, sulfides, phosphides, phosphates, oxynitrides, hydrides, borocarbonitrides [5-8]. Remarkably, HEMs show a high entropy stabilization effect, meaning that in HEM crystal structure, it is possible to dissolve also species with a different crystal structure, which alone cannot be stable in the HEM's crystal structure, thus opening new opportunities in extending the boundaries of crystal stability and of functional characteristics and their control [9-11].

The subclass of high entropy metal diboride (HEDB) ceramics are studied as promising superhard and ultra-high temperature materials with outstanding mechanical, oxidation, and radiation shielding properties [5, 12-18] or as superconductors [19]. The crystal structure is hexagonal, typical of AlB_2, and it is composed of graphene-like layers of B stacked in the *c*-axis direction with alternating layers of mixed metal atoms. For ultra-high temperature applications (≥ 2000 °C), metals in HEDB are selected from groups IV, V, and VI, considering that the individual diborides have high melting temperatures close to 3000 °C or above [20]. They are also hard and oxidation-resistant. When compared to single or bi-metal diborides, HEDBs have better mechanical properties for specific conditions. For example, at room temperature, HEDBs are superior from the hardness viewpoint [8, 17, 21-23]. These HEDBs are single phase as observed by X-ray diffraction. The general trend is that the scientific community's efforts are currently focused on synthesizing and characterizing single-phase HEDB. However, in some HEDBs, phase segregations [17, 21, 22, 24-27] were detected by scanning electron microscopy (SEM). The segregations usually had the AlB_2 crystal structure, e.g., one-metal-rich solid solutions such as the Nb-rich phase in $(Hf_{0.2}Nb_{0.2}Ta_{0.2}Ti_{0.2}Zr_{0.2})B_2$ from ref. [24], or bimetallic $(Ta_{0.5}Ti_{0.5})B_2$, $(Hf_{0.5}Ti_{0.5})B_2$, and single metal HfB_2 in $(Hf_{0.2}Mo_{0.2}Ta_{0.2}Nb_{0.2}Ti_{0.2})B_2$ from ref. [28]. Phase $(Ti_{1.6}W_{2.4})B_4$ was observed by XRD in $(Mo_{0.2}Zr_{0.2}Ta_{0.2}Nb_{0.2}Ti_{0.2})B_2$ from ref. [17]. A W-rich phase was present in $(Hf_{0.2}Mo_{0.2}Ti_{0.2}W_{0.2}Zr_{0.2})B_2$ from ref. [21], while WB was identified in XRD patterns taken on $(Hf_{0.2}Mo_{0.2}Ti_{0.2}V_{0.2}W_{0.2})B_2$ in ref. [14]. In addition, metal oxides were also found in HEDBs [5]. Hence, for a given composition, the reported HEDBs can be very different in terms of homogeneity, being closer or not to a single phase HEDB, and in some cases, they can be identified with a composite composed of a HEDB matrix with reinforcement of precipitates. It is obvious that the AlB_2-type solid solution phases in the HEDB material and the presence of precipitates, as well as the microstructural features (size, size distribution, morphology, boundaries, pores, structural defects, micro-strain) and the relationship between the components will play an important role in defining the mechanical properties.

Currently, hardening in a fully dense HEDB is attributed to solid solution hardening and disorder among the transition metal species. These mechanisms promote higher hardness values than predicted from the properties of the constituents with the volumetric rule of mixtures calculation [17, 29-33]. Nevertheless, for the assessment of different mechanical properties, contributions from other deformation mechanisms, e.g., of those active in ceramics and composites, should not be neglected as the interplay between the intrinsic features of the constituents and the interaction between them is of paramount importance. Therefore, in the last years, attention has also been paid to non-equimolar HEDB and to HEDB composites. The non-equimolar $(Zr_{0.225}Hf_{0.225}Mo_{0.225}W_{0.1})B_2$ HEDB was reported to exhibit a high Vickers hardness of 27.5 GPa at a load of 1.96N [34]. The non-equimolar $(Zr_3Ta_2Nb)B_2$ MEDB had a high bending strength of 700±50 MPa at room temperature and 500 ± 50 MPa at 1600 °C, these values being ~1.7 times higher than for ZrB_2. At higher temperatures, bending strength rapidly decreased, and at 2000 °C, they displayed values similar to ZrB_2 (180 - 200 MPa) [35]. HEDB

composites with SiC, B_4C, Ni, high entropy carbides, etc., show promising results being reviewed in refs. [5, 8, 13].

The previous paragraphs indicate that incomplete or multiphase solid solutions, non-equimolar metals, and composite HEDBs are of much interest and deserve further attention. These aspects are especially important considering that diboride ceramics are brittle (fracture toughness < 4.8 MPa·$m^{1/2}$ in HEDB [13]), they retain this feature up to high temperatures, and mechanical properties such as bending strength (measured in Ar or air) are usually suppressed (down with 20-50% at temperatures above 1000-1500 °C) with the increase of temperature [36-49]. An ideal situation would be maintaining or increasing the strength and providing sufficient ductility with increasing working temperature. This is counter-intuitive since a higher temperature promotes material softening, enhances ductility, usually through creep and grain boundary sliding, and automatically decreases strength. It is remarkable that there are signals from the literature that diboride ceramics and composites with special microstructures can at least partially overcome the shortcomings indicated. Some examples in this regard where at least one diboride is present in the material are presented in the next paragraph.

The bending strength (in Ar) of NbB_2 ceramic containing hexagonal BN (h-BN) impurities from ref. [41] remained unchanged up to 1600 °C, slightly increased at 1700 °C, and finally decreased at 1800 °C, showing at this temperature plastic deformation and being accompanied by h-BN disappearance. Composites of NbB_2-CrB_2 have high oxidation resistance and hardness [50]. Eutectic B_4C-NbB_2 and SiC-NbB_2 composites exhibit room-temperature high fracture toughness (7 MPa·$m^{1/2}$) and hardness (25-30 MPa) [51-53]. At the same time, the SiC-NbB_2 eutectic maintains a high flexural strength of 600 MPa up to 1900 °C. Ceramic composite ZrB_2-TaB_2 (44 wt.% TaB_2) does not experience a decrease in bending strength up to 1000-1200 °C and the decrease at 1600 °C provides a strength value that is considerably higher than for ZrB_2 [54]. Reactively spark plasma sintered ceramic from powder mixtures of ZrB_2, Ta, and amorphous boron produced a composite composed of a Ta_3B_4 chain-like mesh with islands of ZrB_2, ZrB, TaB and (Zr, Ta)B_2 phases [40]. This material preserved its bending strength (in Ar) quite well, up to 2000 °C. At this temperature, the bending strength was close to 400 MPa, i.e., comparable to room temperature values for ZrB_2. At 2000 °C, plastic deformation occurred, and it was amplified for a higher bending load (2.5 mm/min compared to 0.5 mm/min). Composite specific structure and formation of (Zr, Ta)B_2 solid solution were mentioned as the reason for mechanical properties improvement. The bending strength of the B_6O-TaB_2 ceramic composite slightly increases up to 800 °C, remains constant up to 1600 °C, and rapidly decreases at 1800 °C due to the decomposition of boron suboxide [42]. Plastic behavior was observed during bending at 1800°C. In TiB_2-TaC ceramic [39] the decay of bending strength (in Ar) with temperature up to 1600 °C is not suppressed, but it is significantly lower than for TiB_2 or TaC. Evidence for very limited local plastic deformation was noted in the sample after performing bending at 1600 °C. This result suggests that the brittle-plastic transition temperature of this TiB_2-TaC composite was higher than for individual TiB_2 and TaC phases. The main cause was considered the development of the (Ti, Ta)(C, B) phase. In another composite, TiB_2-B_4C, simultaneous strengthening, and large fracture strains due to a plastic-like contribution was recorded at 1800 and 2000 °C. Bending strength at 1600 °C was below 1 GPa, exceeded 1GPa at 1800 °C [55] and was in the range of 1.2-8.4 GPa at 2000 °C [56]. The main reasons were considered to be related to B_4C, namely a rearrangement mechanism at 1800 °C of stacking faults and twins in a process of mechanical energy absorption driven by a shear stress and an amorphization mechanism active at 2000 °C. Authors also noted that the role of TiB_2 was not clarified, yet.

In summary, diborides containing Ti, Ta, Hf, Zr, Nb have a high potential for outstanding ultra-high-temperature mechanical properties. By taking into account the already addressed relevant results, in this work, we fabricate by spark plasma sintering from mixtures of single-metal diboride powders a HEDB with equimolar composition $(Ti_{0.25}Ta_{0.25}Hf_{0.25}Zr_{0.25})B_2$. Metals are written in the order of their atomic sizes in diborides [20]. This composition was selected based on our previous experience with fabrication by spark plasma sintering (SPS) of a $(Ta_{1/3}Hf_{1/3}Zr_{1/3})B_2$ MEDB [4]. This MEDB material is composed of two diboride phases and has shown a bending strength of 310 ± 42 and 318 ± 14 MPa at room temperature when spark plasma sintered at 1927 °C for a dwell time of 1 and 20 min, respectively. These values are slightly lower but quite close to 339 ± 17 MPa in (Ti, Ta, Hf, Zr, Nb)B_2 HEDB [57]. Therefore, the presence of extra atoms of Ti and Nb in HEDB compared to MEDB may question the

idea that, in the case of bending, the effects of solid solution and disorder on bending strength when moving from MEDB to HEDB are as strong and relevant as expected and, consequently, it may suggest that other contributions can have a weighty share. To approach this idea, we focus in this article on bending behavior up to temperatures of 2000 °C and fractography details of the $(Ti_{0.25}Ta_{0.25}Hf_{0.25}Zr_{0.25})B_2$ HEDB. The material was thought as a HEDB with Ti and without Nb since: (i) Ti has the smallest atomic radius among all considered metals Ti, Ta, Hf, Zr, and Nb. Hence, it can be easily accommodated in the AlB_2 crystal structure [20]. This observation suggests the idea that processing conditions established for MEDB [4] can be used for fabrication of the indicated HEDB, thus enabling the direct comparison between MEDB and HEDB; (ii) TiB_2 has the lowest melting point among the Ti, Hf, Zr, or Nb diborides. Expectations are that the differences among the diborides will promote microstructures with high strength and convenient plasticity at high temperatures; (iii) For systematics, we deliberately avoided the introduction of the fifth element, Nb, in our composition, leaving it to future works. Moreover, as mentioned above, Nb has shown a marked tendency towards segregation in $(Ti_{0.2}Ta_{0.2}Hf_{0.2}Zr_{0.2}Nb_{0.2})B_2$ [25]. The $(Ti_{0.25}Ta_{0.25}Hf_{0.25}Zr_{0.25})B_2$ HEDB material obtained and investigated in this work is shown to have peculiar heterogeneity at nano and micro scales. These features are discussed as being essential for its remarkable mechanical properties. Deformation resistance under bending load is enhanced from room temperature up to 1800 °C. Although at 2000 °C, bending strength decreases, its value is still ~ 25 % higher than at room temperature. At 2000 °C, a ductile behavior with a deformation strain of ~7.5% occurs. We also note that to the authors' knowledge, bending experiments on HEDBs at elevated temperatures were not reported in the literature.

2. Experimental

Raw materials were commercial powders of TiB_2 1-2 µm (Lot AWP6545, Wako Pure Chemicals, Osaka, Japan), TaB_2 1-5 µm (Lot #T301160, Japan New Metals Co. Ltd., Osaka, Japan), HfB_2 1-3 µm (Lot # T302510, Japan New Metals Co. Ltd., Osaka, Japan) and ZrB_2 1.5-2.5 µm (Lot# TLN0199, Wako Pure Chemicals, Osaka, Japan). Information regarding the morphology of the raw powders TiB_2, TaB_2, HfB_2, and ZrB_2 is available in refs. [4, 58, 59].

Raw diboride powders were mixed with an Intelli-Mixer RM-2M (ELMI, Latvia) in an equimolar ratio TiB_2:TaB_2:HfB_2:ZrB_2 = 1:1:1:1. This procedure does not use solvents and grinding of materials does not occur or is limited. The mixing process occurs through fast vibration of the powders in relatively small volumes (50 ml). In the first step, we mixed light diborides TiB_2 and ZrB_2 for a higher vibration regime. Next, in the second mixing step, we added HfB_2, and in the third one, the heaviest boride TaB_2 was introduced, lowering the vibrations mode in each step. The total mixing time in each step was 20 h (5 x 4 h). To avoid overheating above 50 °C the mixer after four hours of vibrations, the process was stopped for 2h. A similar approach was used for the fabrication by SPS of a composite-like ceramic in the ZrB_2-B system with good mechanical temperature-dependent properties [40].

The four diboride powder mixtures were loaded into a graphite die and punches system and processed by spark plasma sintering (SPS) with a 'Dr. Sinter' 1050 (Sumitomo, Japan) equipment. Samples were disks with a diameter of 30 mm. The SPS thermal schedule was composed of four steps: (1) heating to 700 °C in four minutes with a five-minute dwell; (2) heating to 1400 °C in 10 min and a 5-minute hold; (3) heating to 1927 °C in five minutes and (4) holding at this temperature for 20 min; (5) cooling down to 600 °C in 15 min and further furnace cooling to room temperature (RT). Steps (1) and (2) were performed in a vacuum (initial vacuum of ~2 Pa). During the dwell at 1400 °C, Ar was introduced in the SPS furnace, exceeding 1 atm for a flow rate of 2L/min. The initial uniaxial load on the sample was 8 kN, which was increased at the end of step (2) to 12 kN. The uniaxial load was continuously increased up to 32 kN, attaining this value at the beginning of step (4), and it was maintained constant during steps (4) and (5). A sample was extracted from the die, and graphite and C-contaminated surfaces were removed with rough polishing. Samples were cut into 2 x 2.5 x 20 mm rectangular bars with a diamond disk. Steps in SPS were designed considering the removal of boron oxides [60] inherently present on the surface of the diboride raw powders and the thermal stabilization of the SPS process. Uniaxial pressure is low at low temperatures but enough to ensure good electrical

contact between graphite punches and sample. At high temperatures, uniaxial load is increased and maintained, thus ensuring good densification of the sample. Polishing was performed with diamond paste down to 0.5 μm on all surfaces to remove defects as possible flaws in bending strength experiments.

Three-point bending tests in Ar atmosphere at different temperatures from RT up to 2000 °C were conducted with Shimadzu AG-X plus system (Shimadzu, Japan) according to JISR 1604 [61] corresponding to ASTM C1211-13 [62]. The span was 16 mm, and the loading rate was 0.5 mm/min. The heating schedule to bending temperature was from RT to reach 200 C in 10 min, and from this temperature to testing temperature, heating was performed at a rate of 18 °C/min. The bending load was applied after maintaining the sample for 5 min at the testing temperature. Cooling after testing was done at a rate of 20 °C/min. The bending strength was averaged for 2-5 tested samples for each bending temperature, and the standard deviation was taken as the measurement accuracy.

After bending experiments, samples were measured by X-ray diffraction (XRD) with a D8 Advance (Bruker, Germany) diffractometer ($Cu_{K\alpha}$ radiation).

Microscopy observations were made with the scanning electron microscope (SEM) Tescan Lyra 3XMU (Germany) equipped with an energy dispersive spectroscopy (EDS) detector and a focused ion beam (FIB) facility and with the transmission electron microscope (TEM) JEOL 2100 (Japan). The samples for TEM were fabricated by the standard cross-sectional (XTEM) method with ion milling (GATAN Precision Ion Polishing System). TEM samples were obtained from the fractured area.

The bulk density of the SPSed samples was 98.5%, as measured by the Archimedes method using toluene as a medium in accordance with ASTM B B962-23[63].

3. Results and Discussion

3.1 Bending test experiments

Strength-strain (σ - ε) bending curves are presented in Fig. 1a. Bending strength at RT is 326 ± 22 MPa, corresponding to a fracture strain of 0.93%. Fracturing is elastic, behavior being brittle. There are no signs of significant plastic deformation. The bending strength value is comparable with the values of 310 ± 42 or 318 ± 14 MPa for $(Ta_{1/3}Hf_{1/3}Zr_{1/3})B_2$ MEDB [4], and it is higher than for individual diborides.

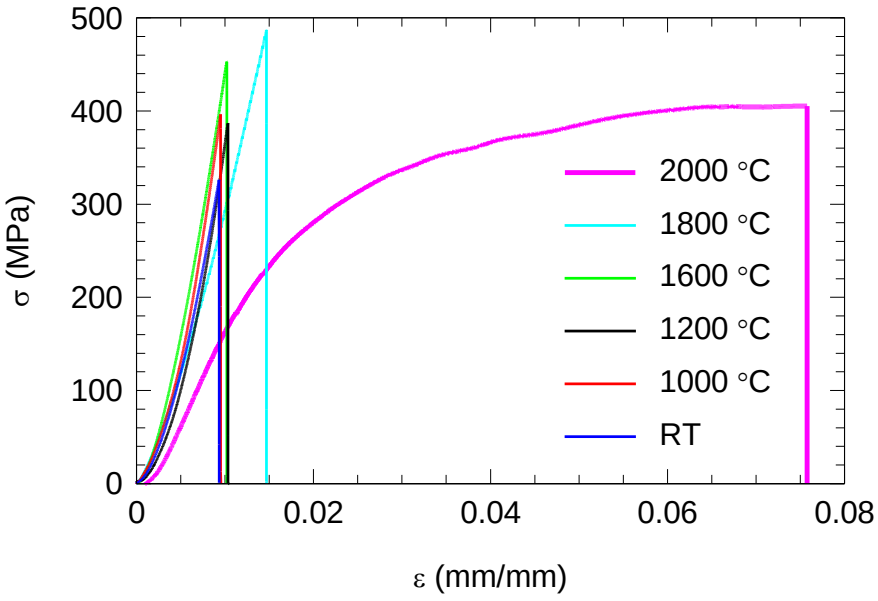

(a)

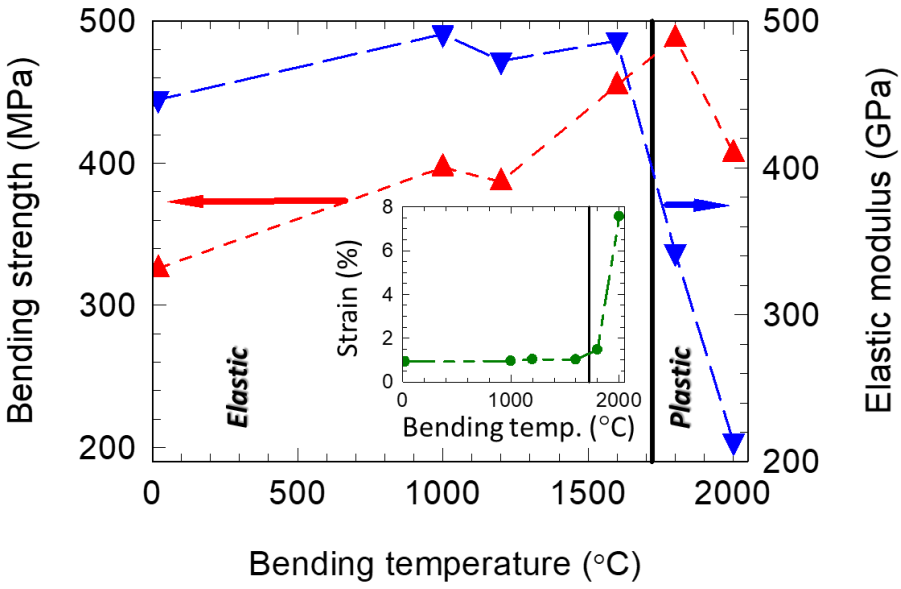

(b)

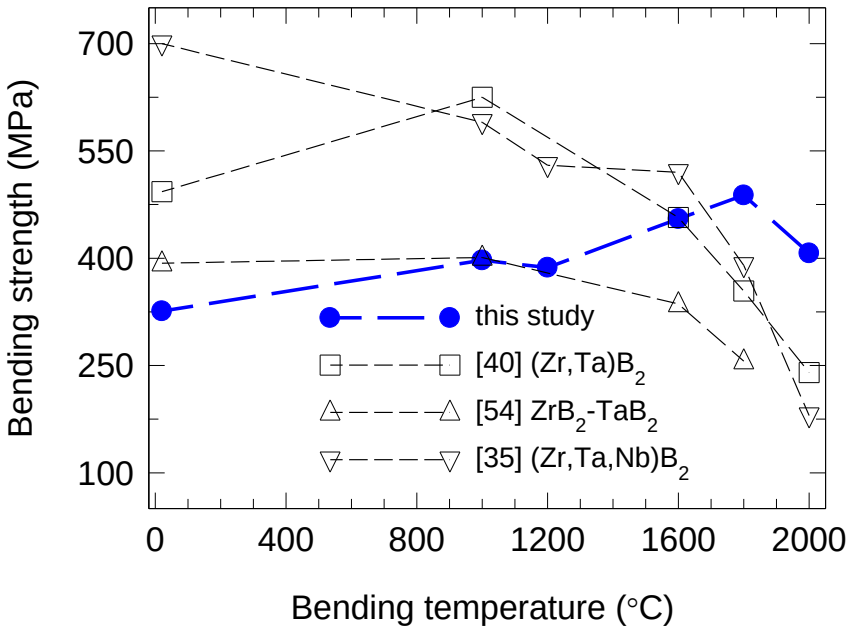

(c)

Fig. 1 (a) - Stress-strain bending curves of the $(Ti_{0.25}Ta_{0.25}Hf_{0.25}Zr_{0.25})B_2$ HEDB, tested at different temperatures; (b) Temperature dependence of bending strength, elastic modulus *E*, and bending strain (inset). Elastic and plastic deformation regions at temperatures below and above ~1700 °C, respectively, are indicated. (c) Comparison of bending strength curves vs. temperature for different diboride materials.

From RT up to 1600 °C, HEDB preserves the elastic behavior. One notable difference (Fig. 2b) is the enhancement of the bending strength up to 455 ± 19 MPa, i.e., with about 38%. At the same time, elastic modulus (*E*), determined as the slope of the linear part of the stress-strain curve [64], shows a relatively low variation in the 448 - 490 GPa range (Fig. 2b). Bending strain also has a low variation being between 0.93 and 1.03 %. In comparison with ref. [65] the HEDB with composition $(Ti_{0.2}Zr_{0.2}Hf_{0.2}Nb_{0.2}Ta_{0.2})B_2$ obtained by hot pressing has 339 MPa bending strength at RT, i.e. it is similar to our material.

At higher temperatures of 1800 and 2000 °C, elastic modulus significantly decreases to 337 and 204 GPa, respectively (Fig. 2b). The decrease of *E* from 1600 to 2000 °C is accompanied by an

increase up to a maximum bending strength value of 488 MPa ± 20 (i.e. with 7.2 % when compared to bending strength at 1600 °C) at 1800 °C followed by a decrease to 407±29 MPa (i.e. with 10.5 % when compared to bending strength at 1600 °C) at 2000 °C. The bending strength at 2000 °C is still remarkably high, with 24.8 % larger than at RT. At 1800 °C, strain is more significant (Fig. 2b inset) due to material softening as indicated by the decrease of *E*, but there is no obvious plastic deformation (Fig. 2a). At 2000 °C strain significantly enhances attaining a value of 7.5 % through plastic deformation (Fig. 2a). Remarkably, at 2000 °C the bending strength has a high value, above the values recorded and reported in literature for other diboride complex materials (Fig. 1c).

Results indicate that there is a strengthening mechanism, and although at bending temperatures of 1800 and 2000 C, the material's softening and, ultimately, plastic deformation is active, strengthening has a strong share of contribution to bending behavior. Actually, the combination of a bending strength higher than at room temperature and considerable plasticity, both determined at 2000 °C, is observed to the authors' knowledge for the first time in the case of a HEDB, thus opening new possibilities for the application of these materials under extreme conditions. To understand the bending effects, in the next Sections, we shall look at the structural and microstructural details of the investigated HEDB.

3.2 X-ray diffraction of the HEDB ceramic after bending test at different temperatures

XRD patterns of the samples after bending test at different temperatures are presented in Fig. 2. Diffraction lines corresponding to AlB2 hexagonal structure and (hkl) planes are indicated [4, 17, 65]. Impurity phases with other structures are not detected. One notes that diffraction peaks are broad and present a shoulder. This indicates that HEDB comprises multiple phases, specifically at least two diboride solid solutions.

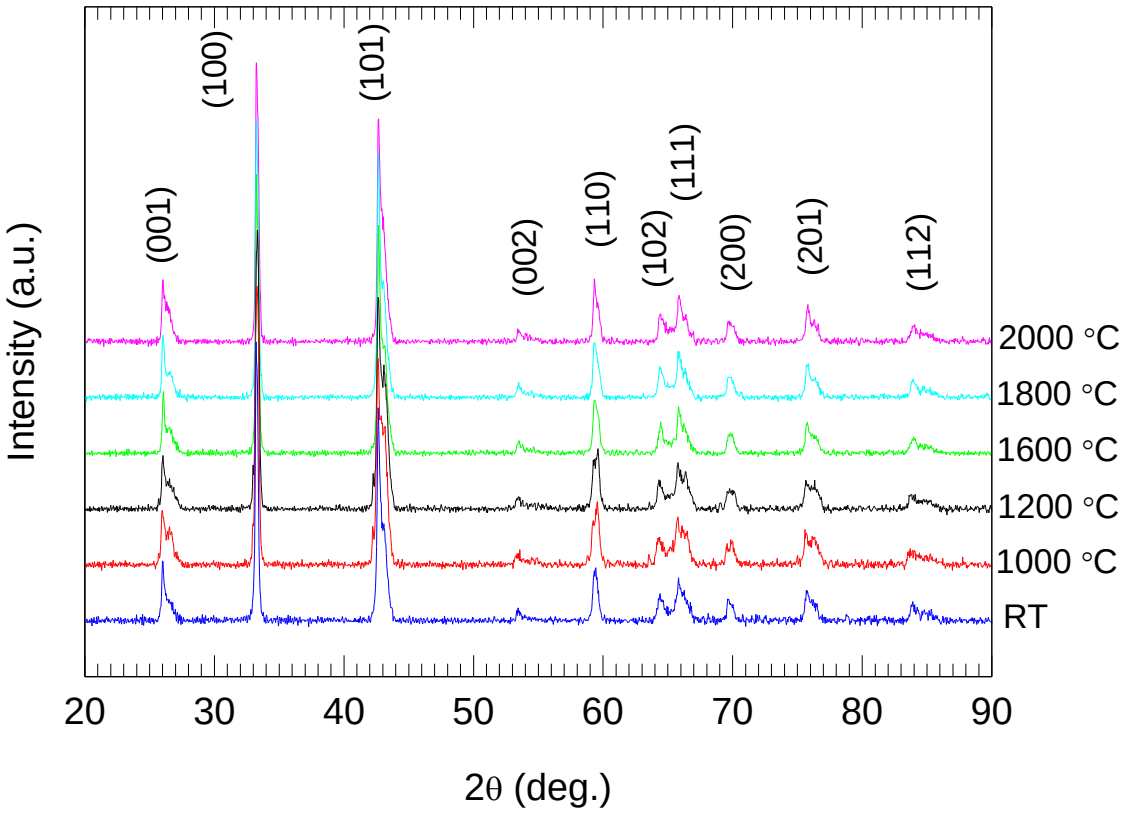

Fig. 2 X-ray diffraction of $(Ti_{0.25}Ta_{0.25}Hf_{0.25}Zr_{0.25})B_2$ HEDB samples after bending test at different temperatures. The (hkl) lines of binary diboride AlB_2-type phases in the Ti-Ta-Hf-Zr-B system are indicated (e.g. binary/ternary phases are: $(ZrTi)B_2$ – PDF 04-011-7056, $(HfTi)B_2$ – PDF 04-011-7057, $(ZrTa)B_2$ – PDF 04-011-7061, $(Ta_{0.7}Hf_{0.3})B_2$ – PDF 04-025-8187, $Hf_{0.34}Zr_{0.33}Ta_{0.33}B_2$ – PDF 04-028-0483).

3.3 SEM fractography aspects of the HEDB ceramic subject to bending tests at different temperatures

Fig. 3 shows SEM images at different magnifications taken of the representative samples after bending at RT, 1000, 1800, and 2000 C.

Cross sections on the fracture surface measured in the secondary electrons (SE) regime show the topography. Samples RT, 1000, and 1800 °C (Fig. 3 a1SE-a3SE) present a surface with a relatively low roughness and with typical appearance for a brittle fracture. The local surface is generally flat on relatively large areas, and even if some irregular wavy structure can be distinguished, there are no abrupt passages between hills and valleys. On the contrary, the sample bent at 2000 °C (Fig. 3 a4SE) displays a sharp and clear step on the fractured surface. This step results from the specific forces that are active during bending and the material's response through a ductile-like breaking. Fractography results are in good agreement with information deduced from strength-strain curves addressed in Section 3.1.

Images measured at low magnification in the backscattering regime (BSE) on the fractured surface (Fig. 3 a1BSE-a4BSE) indicate the presence of at least two phases. Namely, the composite has roughly a microstructure composed of a gray matrix in which there are reinforcing islands of the second phase. We note that the XRD patterns from Section 3.2 indicate the presence of two diboride solid solution phases. In BSE images, heavier materials appear as lighter grey shades.

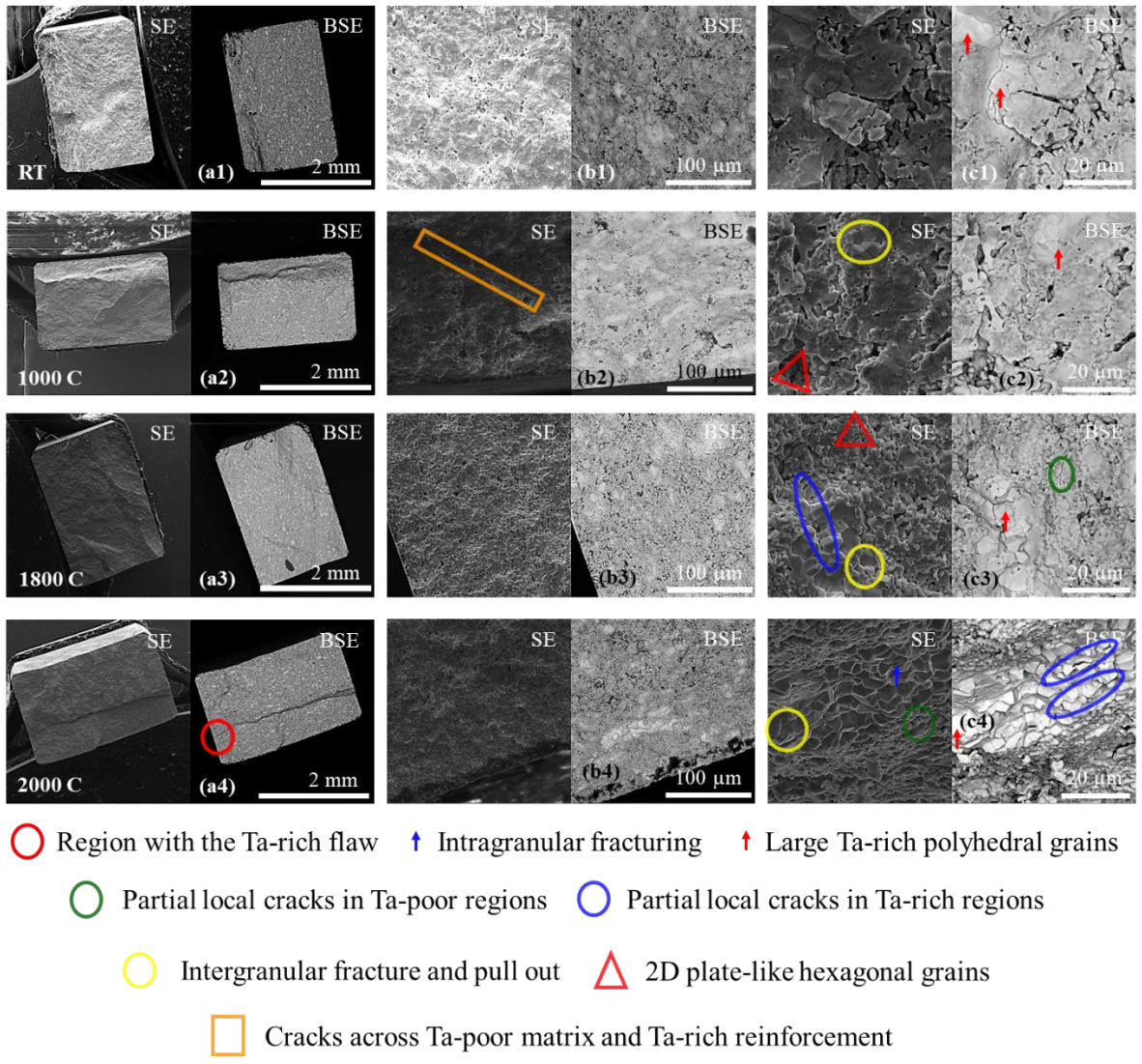

Fig. 3 SEM images in secondary electrons (SE) and backscattering regimes (BSE of the $(Ti_{0.25}Ta_{0.25}Hf_{0.25}Zr_{0.25})B_2$ HEDB samples after bending test at different temperatures. Images (a1)-(a4), (b1)-(b4) and (c1)-(c4) are taken at low (65x), medium (1kx) and high magnifications (4kx).

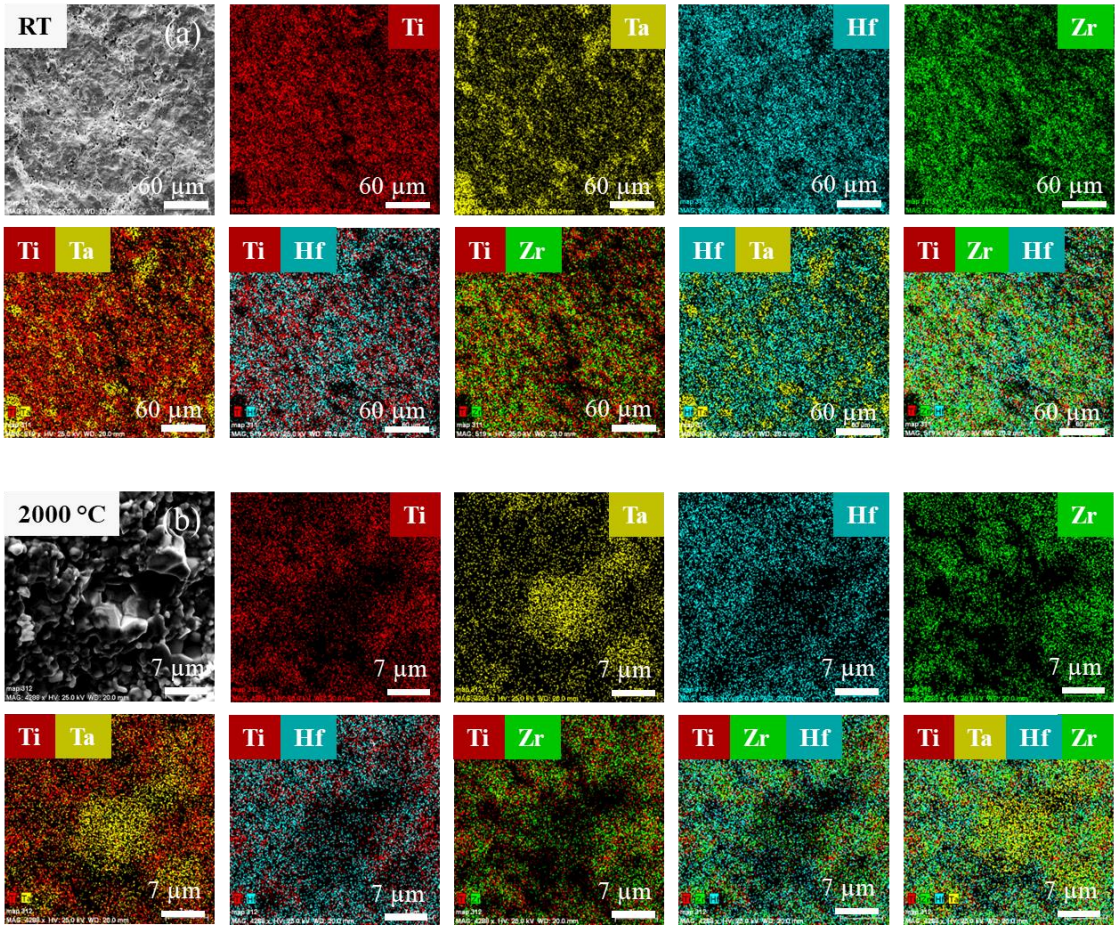

Fig. 4 SEM images, EDS maps and overlapped EDS maps for two, three or four metals of the $(Ti_{0.25}Ta_{0.25}Hf_{0.25}Zr_{0.25})B_2$ HEDB sample after bending test at: (a)- RT and (b)- 2000 °C.

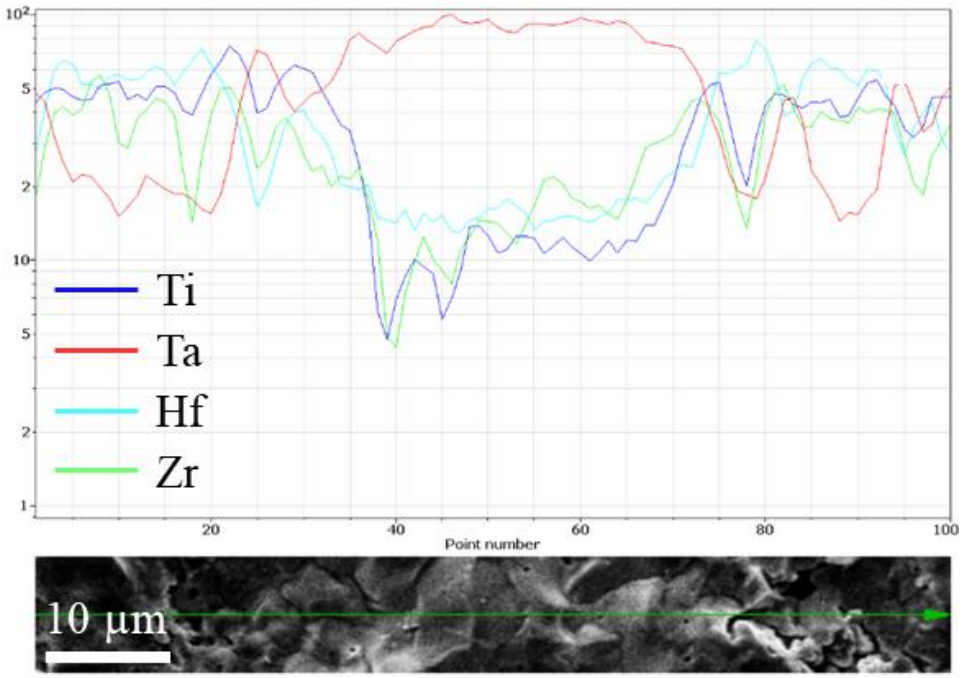

Fig. 5 EDS compositional curves for the component metal elements of the HEDB sample after bending test at RT along the line (green) marked on the SEM image (bottom).

Indeed, EDS maps (Fig. 4) and composition curves of the metals along the measurement line (Fig. 5) highlight the presence of Ta-rich and Ta-poor regions. The average metal composition of the matrix region is $Ti_{0.22}Ta_{0.44}Hf_{0..08}Zr_{0.26,}$ and of the island (reinforcement) Ta-rich region is $Ti_{0.08}Ta_{0.62}Hf_{0.11}Zr_{0.18}$. Boron was detected in both regions, but since it is a light element, its quantitative determination by EDS is not reliable, and due to this, it was not taken into consideration. The most considerable compositional variation is shown by Ti and Ta, and when the amount of one element is high, for the other, it is low and vice versa (Fig. 5). These two elements are the lightest and the heaviest. They have the smallest size (though different) among the component metals of the HEDB [20]. Simple diborides of these elements, TiB_2 and TaB_2 have different melting temperatures of 3230 °C and 3140 °C, respectively. Melting temperatures of HfB_2 and ZrB_2 are 3250 and 3246 °C, i.e., they are closer to the value of TiB_2 than of TaB_2. The relatively small size of Ta, despite being the heaviest atom, and the lowest melting point for TaB_2 prompt us to anticipate an activity of TaB_2 during SPS that stands out from the other diborides. Indicated differences and specific features are important factors influencing interdiffusion and kinetics, which in turn will impact the formation of diboride solid solutions during SPS. It is also worth noting that, to some extent, the compositional variation of Ti is followed by Zr and, to a lesser extent, by Hf, but there are also grains for which this statement is not valid. A closer look at the images of the overlapped EDS maps for two, three, or four metals (Fig. 4) and on the SEM images taken at higher magnifications (Fig. 3 b1BSE-b4BSE and c1BSE-c4BSE) reveals that in each of the two central regions of the HEDB, there are grains with different nuances of grey indicating compositions departing from the above-determined average metal compositions. Therefore, HEDB from this work can be defined macroscopically as a composite where each component, i.e., the matrix and the island-like reinforcement, is made at the nanoscale of different diboride solid solutions (see Section 3.4).

SEM images taken at higher magnification show that Ta-rich island regions are composed of grains with a 3D polyhedral morphology (follow red arrows in Fig. 3 b1SE-b4SE, c1SE-c4SE, and Fig. 6 b, c). This morphology closely resembles that obtained for the bulk samples of TaB_2 sintered by SPS from the raw powder also used in this work [58]. This observation suggests that Ta has a strong influence on the formation of the microstructure and behaves significantly differently during SPS than the other diborides. There is a fraction of relatively big Ta-rich grains of 10-15 µm. Among the raw diboride powders, TaB_2 has the largest particle size of 1-5µm and the encountered differences between the powder and the bulk may indicate a coarsening process during SPS with active participation of TaB_2. The Ta-poor matrix is composed of grains with less defined and rounded edges, and their size is about 1-2 µm or less. Some matrix grains have a hexagonal, and a rather 2D plate-like morphology where occasionally corners with in-plane typical angles of 120 or 60° can be observed (inside red triangles from Fig. 3 c2SE and c3SE). The large Ta-rich grains or clusters act as flaws initiating the material's breakage (see red circle in Fig. 3 a4 and Fig 6 c). Crack propagates through a mixed intragranular (follow blue arrows in Fig. 3 c4SE and in Fig. 6 aSE) and intergranular fracturing mechanism (see yellow circles in Fig. 3 c2SE, c3SE, c4SE and in Fig. 6 cSE). The share of the intergranular fracturing mechanism increases at high temperatures of bending, 1800 and 2000 °C. At 2000 °C this mechanism is dominant and through grain boundary cleavage and pull out of the grains (see yellow circles in Fig. 3 c2SE, c3SE, c4SE and in Fig. 6 cSE) it provides apparent ductility. While this is the typical explanation in the case of a conventional composite, there are interesting peculiar aspects. After bending at 2000 °C material shows the presence of cracks, some of them are locally confined, and, remarkably, they are not protruding from one side to another of the sample, thus preserving material's integrity. We shall call these cracks using the term partial cracks. Partial cracks are interfering with both Ta-rich and Ta-poor regions, as expected for a typical bi-component composite (see orange rectangle in Fig. 3 b2SE and in Fig. 6 bSE). Interestingly, they can also be confined only within one region, Ta-rich (see blue circle/ellipse in Fig. 3 c3SE, c4BSE and in Fig. 6 cSE) or Ta-poor (see green circle/ellipse in Fig. 3 c3BSE, c4SE and in Fig. 6 cSE). In such a case, this should be due to mechanisms of cracks development active within each region, such as cracks' deflection, branching, bridging, and arrest. In other words, each region would behave as a composite.

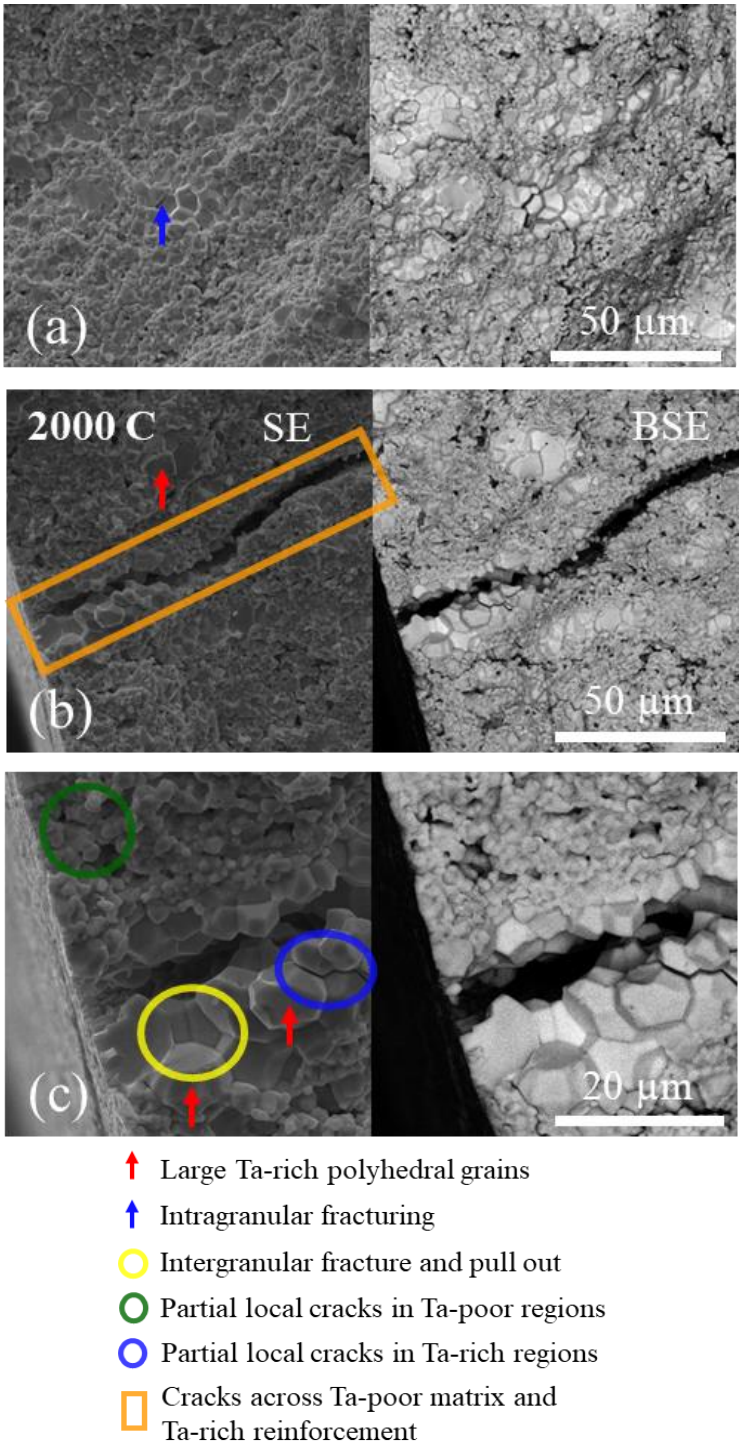

Fig. 6 SEM details of the $(Ti_{0.25}Ta_{0.25}Hf_{0.25}Zr_{0.25})B_2$ HEDB sample after bending test at 2000 °C.

Depending on bending temperature, the composite effects controlling mechanical properties occur due to certain gradients in hardness and toughness among the composite components. For a typical bi-component composite, the indicated gradients are between the matrix and the reinforcement, allowing through their individual response and through their interplay to absorb the mechanical energy introduced in the material in a convenient manner. In the case of our HEDB it is necessary to look for gradients also within each Ta-rich and Ta-poor regions to explain partial cracks presence within matrix or reinforcement. To do so, TEM investigations were employed (see Section 3.4).

3.4 TEM observations on the HEDB samples after bending tests

TEM images and EDS maps taken on the sample after bending at RT are presented in Fig. 7 and Fig.1 Supporting information. There are compositional variations among the grains, but also inside a grain (color intensity in EDS maps or color in the overlapped EDS maps of different metals for one grain may show a significant variation). This is also observed in the Figs. 8 and 9 for the sample after bending at 2000 °C. Within a grain, the interface between regions with different compositions (Fig. 9) is not sharp. It has an irregular shape and is rather compositionally gradual. The last feature promotes some resemblance with functionally graded materials, suggesting that graded grains have similar beneficial and unique properties.

Local EDS quantitative analysis of the metals on the grains (1)-(4) from Fig. 8BF are shown in Table 1. One observes that at the nanoscale, there are compositions, e.g. (1), with a high and low amount of Ti and Ta, the ratio r being 38.83/7.60 = 5.1, but there are also compositions more balanced and closer to 1 (e.g. for (2) r = 12.21/7.83 = 1.56 and for (4) r = 19.23/19.38 = 0.99. However, other elements can show large deviations for balanced compositions with respect to Ti and Ta. In compositions (2)-(4), the amount of Hf is high (4.6 and 7.3 times greater than for Ti and Ta, respectively). The lowest variation is apparently for Zr. The grains (1)-(4) are from the Ta-poor matrix defined and observed in section 3.3.

Matrix presents sintered grains with closed pores. Pores size is typically in the range of a few hundred nm. These nanopores on the edge may show the presence of oxygen, but this oxygen may not fill in the entire contour of the pore edge (Fig. 8a, map for oxygen). This localized oxygen suggests that no reaction with oxygen occurred during SPS, and oxygen is a low-level impurity originating from the surface of the raw powders. In literature, oxygen presence in HEDB is reported, sometimes attaining considerable concentrations. In such cases, oxygen is considered a factor that suppresses densification and mechanical properties [5, 66]. In our work, the high level of mechanical properties (Section 3.1) and their remarkable behavior with temperature indicate that the influence of the pores is reduced or eliminated by other much stronger positive factors and, thus, can be neglected.

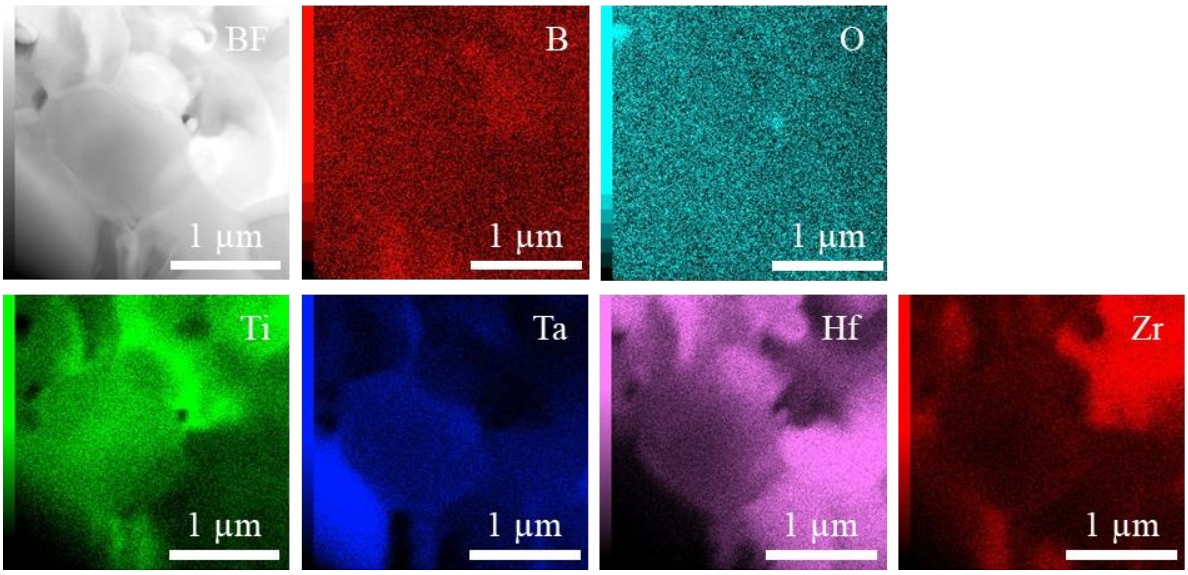

Fig. 7 TEM elemental map images of Ta-Zr-Hf-Ti HEDB sample after bending test at RT.

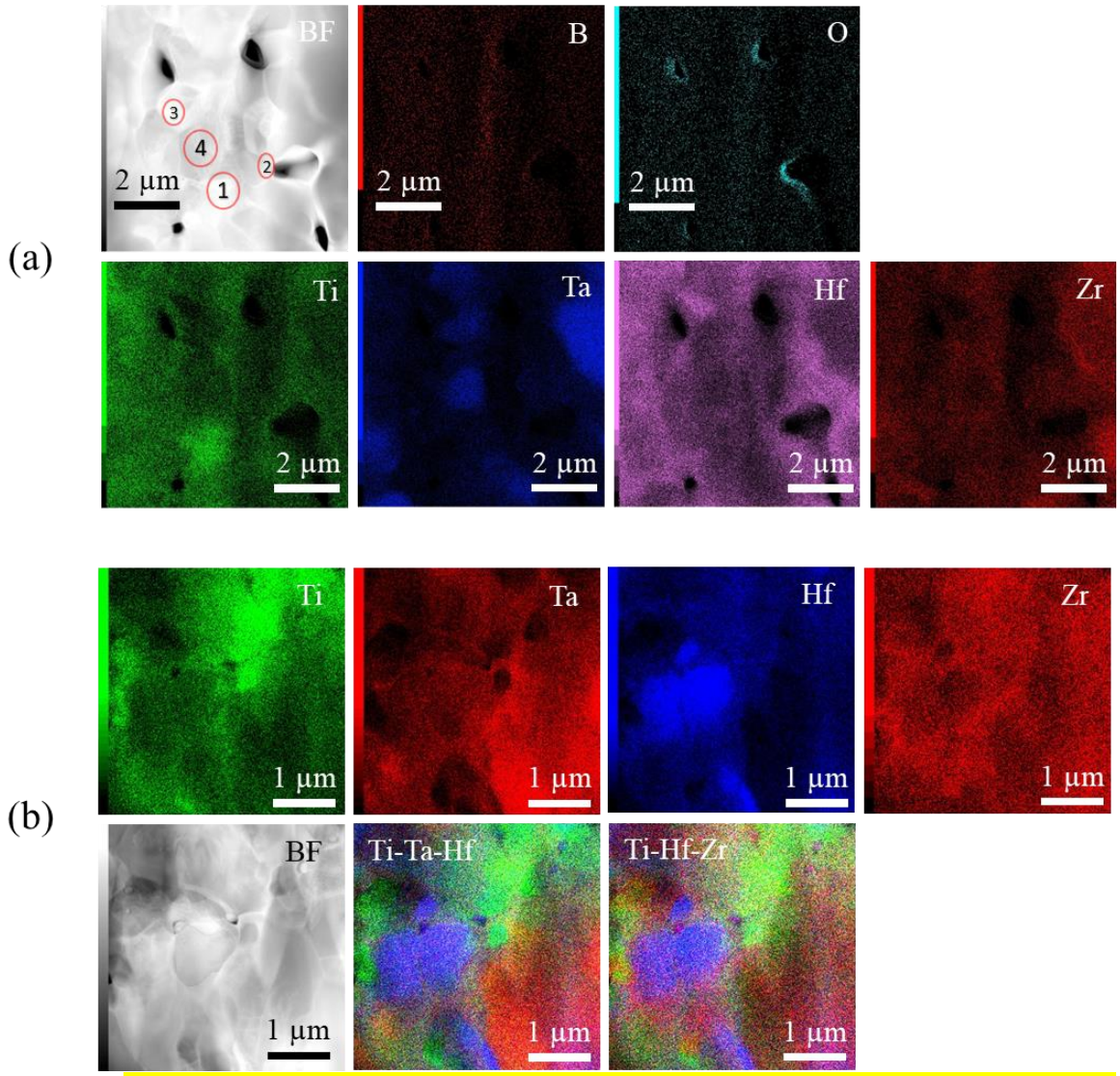

Fig. 8 TEM image, elemental maps, and overlapped elemental maps for Ti, Ta, Zr, and Ti, Hf, Zr on the fractured HEDB cross section after bending at 2000 °C.

In Fig. 9, a large grain from the sample is observed after bending at 2000 C. The grain has two regions. Region (A) is Ti-poor and Ta-rich, while region (B) is Ti-rich and Ta-poor (Table 1). One also observes that the grain has dislocations extending over both regions. More dislocations are in region (A) than in region (B). This can be an indication of a different response of the two regions to mechanical load and suggests that there is a scattering of the elasto-plastic properties between the two regions.

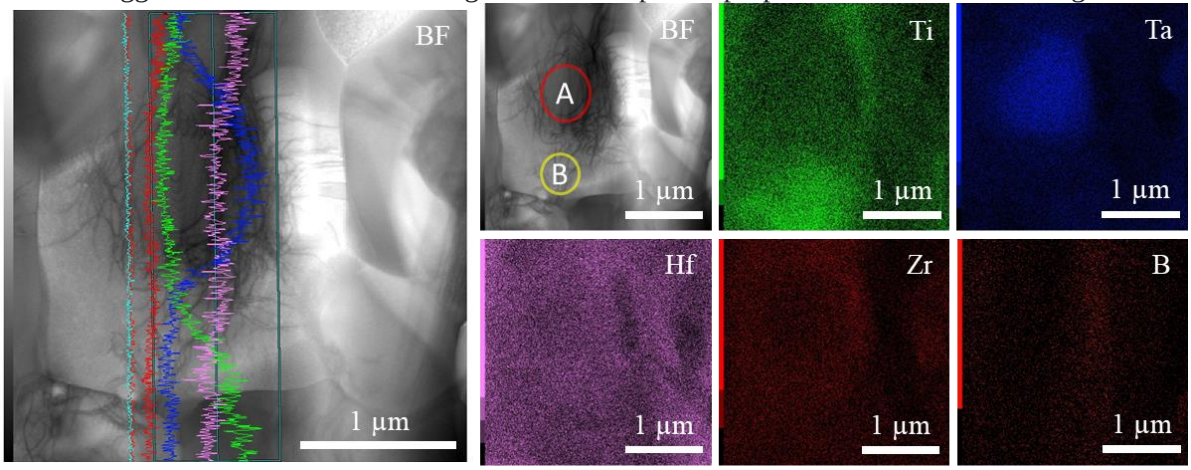

Fig. 9 TEM image (left) and elemental maps of Ti, Ta, Hf and Zr measured on the HEDB sample after bending at 2000 °C.

Table 1. Local EDS results taken at locations (1)-(4) from Fig. 8 and (A) and (B) from Fig. 9.

Location	**(1)**	**(2)**	**(3)**	**(4)**	**(A)**	**(B)**
Element	at. %	at. %	at. %	at. %	at. %	at. %
Ti (K)	38,83	12,21	18,37	19,23	12,63	26,24
Zr (K)	23,07	22,14	27,88	29,40	25,04	28,79
Hf (L)	30,50	57,81	42,00	31,99	26,94	35,97
Ta (L)	7,60	7,83	11,75	19,38	35,39	9,00
Total	100	100	100	100	100	100

Combined results of SEM and TEM show that HEDB from this work has a complex structure extending from nano to micro scales. Local compositional variation is suitable to better tolerate mechanical load amplitude and increase, which takes place in a more extensive temperature range. The absorbance of mechanical load energy seems more significant, avoiding the high brittleness typical for a single component diboride ceramic and significantly expanding the ductility at the right high temperature (in this work at 2000 C) in a way that is not possible for a single-phase material, or even for a two phases conventional composite. In literature, there are works demonstrating significant plasticity of small ceramic samples under compressive load and at RT. Examples are diamond, MgO, SiC, and different nano-grained ceramics [67-74]. Our multiphase HEDB can be viewed as a massive macroscopic bulk that can take advantage of and respond to load as nano ceramic samples. The current understanding is that the behavior of the small nano ceramic samples is replicated in the multiphase macroscopic HEDB. This is due to the presence of nanograins and regions, due to their variable composition favorably distributed in the macroscopic sample, and due to the presence and behavior of gradual interfaces and dislocations. These features can ensure the transfer at a high bending temperature of 2000 °C of the desired plastic behavior from nano to macro scale and activation of dislocation plasticity while strength remains high and still significantly exceeds the RT value. At the same time, mechanisms describing the mechanics of microstructured composites [75] are also active but are influenced and complemented by the nano contribution: strengthening up to 1600 C can be related mostly to residual strain-relaxation, this being also aided by specific nano/microstructure. Presented scenario, details, and explanations need further research. One possibility is the occurrence of phase transitions, which might be suggested by significant changes in mechanical properties at 2000°C. Authors of ref. [76] indicate that simple diborides with AlB_2 structure do not show phase transitions with temperature unless high pressures are applied. Similar information about diboride solid solutions is not available. The maximum uniaxial pressure during SPS and bending strength values are at least one order of magnitude lower than the pressures needed for phase transitions. In SPS, the punch displacement, which is equivalent to the shrinkage of the sample height, was measured in situ as a function of time or temperature. These curves did not show unusual features suggesting phase transitions. However, in some diboride, solid solutions such as $(Ti, Cr)B_2$, the thermal expansion coefficients measured by XRD up to 1727 °C do not obey the rule of mixture [77].

4. Conclusion

A mixture of individual metal diborides prepared under certain conditions was spark plasma sintered to obtain a high entropy four-metal diboride $(Ti_{0.25}Ta_{0.25}Hf_{0.25}Zr_{0.25})B_2$. XRD, SEM, and TEM characterization were performed, and the results indicate the complex structure of this material. At the microscale, the material resembles a composite. The reinforcement consists of grains that are rich in

tantalum (Ta) and poor in titanium (Ti), while the matrix is made up of grains that are rich in titanium and poor in tantalum. Apparently, Ta, through the lowest melting temperature of TaB_2 and its relatively small atomic size in the diboride, plays the most active role in microstructure formation and mechanical properties. Studies at the nanoscale reveal significant compositional variations among grains and within different regions of a single grain. The interface is gradual and has an irregular shape. Consequently, the HEDB in this work exhibits characteristics similar to functionally graded materials and complex composites. As a complex composite, it features a specific nanostructured arrangement that forms a micro-scale structure defined by a matrix and an island-type reinforcement. The term 'composite within a composite' hints at this HEDB, but it is ambiguous and does not fully convey the details.

Depending on temperature, the unique HEDB structure at nano and micro scales generates special, outstanding mechanical properties. A significant finding is that at high temperatures up to 2000 °C, the HEDB effectively responds to bending loads, demonstrating deformation-resistant behavior. This creates new opportunities for utilizing these materials in extreme conditions. Up to temperatures of 1800°C, the dominant effect is strengthening, contributing to an essentially elastic behavior. At 1800 °C, the bending strength reaches a maximum of 488 MPa, which is almost 50% higher than the room temperature value of 326 MPa. At 2000 °C, the bending strength decreases to 407 MPa. It can be observed that the percentage is still significantly higher at 25% compared to the value at RT. The bending strength value at 2000 °C is higher than the reported data from the literature for other diboride complex materials. It is particularly interesting that high bending strength at 2000°C is accompanied by notable ductile behavior, characterized by a strain of 7.5% before the sample breaks. In addition to the contributions from solid solution, heterogeneity, and conventional composite effects to the mechanical response, the results also indicate a significant role of dislocations, particularly during the dominant plastic deformation process at 2000°C. Further experimental and theoretical studies are needed to enhance understanding of specific mechanical properties.

Author contributions:

We confirm that the manuscript has been read and approved by all named authors and that no other persons satisfied the criteria for authorship but are not listed. We further confirm that all have approved the order of authors listed in the manuscript.

Conceptualization, P.B., and OV; Methodology, all authors; Investigation, all authors; Formal analysis, all authors; Validation, P.B., and O.V.; Writing—original draft preparation, P.B.; Writing—review and editing, O.V.; Visualization, P.B., and M.A.G.; funding acquisition, P.B., and O.V.; Supervision, P.B., and O.V..

Acknowledgments

P.B., M.A.G., and A.K. acknowledge UEFISCDI for partial support through Core Programs PC1-PN23080101 and PC2-PN23080202. O.V. acknowledges the KAKENHI C 24K08035 Grant in Aids of Scientific Research for partially supporting this study.

Competing interests

We, the authors, declare no competing interests.

References

[1] B. Cantor, I. T. H. Chang, P. Knight, A. J. B. Vincent, Microstructural development in equiatomic multicomponent alloys. *Mater Sci. Eng. A* **2004**, 375–77, 213–218. https://doi.org/10.1016/j.msea.2003.10.257.

[2] J. -W. Yeh, S. -K. Chen, S. -J. Lin, J. -Y. Gan, T. -S. Chin et al. Nanostructured high-entropy alloys with multiple principal elements: novel alloy design concepts and outcomes. *Adv. Eng. Mater.* **2004**, 6, 299–303. https://doi.org/10.1002/adem.200300567.

[3] D. Demirskyi, T. Nishimura, T. S. Suzuki, Y. Sakka, O. Vasylkiv et al. High-temperature toughening in ternary mediumentropy $(Ta_{1/3}Ti_{1/3}Zr_{1/3})C$ carbide consolidated using spark-plasma sintering. *J. Asian Ceram. Soc.* **2020**, 8, 1262–1270. https://doi.org/10.1080/21870764.2020.1840703.

[4] D. Demirskyi, T. S. Suzuki, K. Yoshimi, O. Vasylkiv, Synthesis of medium-entropy $(Zr_{1/3}Hf_{1/3}Ta_{1/3})B_2$ using the spark plasma consolidation of diboride powders. *J. Ceram. Soc. Jpn.* **2020**, 128, 977-980. http://doi.org/10.2109/jcersj2.20151.

[5] L. Feng, W. G. Fahrenholtz, D. W. Brenner, High-Entropy Ultra-High-Temperature Borides and Carbides: A New Class of Materials for Extreme Environments. *Annu. Rev. Mater. Res.* **2021**, 51, 165–85. https://doi.org/10.1146/annurev-matsci-080819-121217.

[6] C. Oses C. Toher, S. Curtarolo, High-entropy ceramics. *Nat. Rev. Mater*. **2020**, 5, 295–309. https://doi.org/10.1038/s41578-019-0170-8.

[7] R. Z. Zhang, M. J. Reece, Review of high entropy ceramics: design, synthesis, structure and properties. *J. Mater. Chem. A* **2019**, 7, 22148–22162. https://doi.org/10.1039/C9TA05698J.

[8] S. Akrami, P. Edalati, M. Fuji, K. Edalati, High-entropy ceramics: Review of principles, production and applications. *Mat. Sci. Eng. R.* **2021**, 146, 100644. https://doi.org/10.1016/j.mser.2021.100644.

[9] M. Gaboardi, F. Monteverde, F. Saraga, G. Aquilanti, L. Feng, et al. Local structure in high-entropy transition metal diborides. *Acta Materialia* **2022**, 239, 118294. https://doi.org/10.1016/j.actamat.2022.118294.

[10] C. M. Rost, E. Sachet, T. Borman, A. Moballegh, E. C. Dickey, et al. Entropy-stabilized oxides. *Nat. Commun.* **2015**, 6, 8485. https://doi.org/10.1038/ncomms9485.

[11] C. M. Rost, Z. Rak, D. W. Brenner, J. -P. Maria, Local structure of the $Mg_xNi_xCo_xCu_xZn_xO$(x=0.2) entropy-stabilized oxide: An EXAFS study. *J. Am. Ceram. Soc.* **2017**, 100, 2732-2738. https://doi.org/10.1111/jace.14756.

[12] S. Iwan, C. -M. Lin, C. Perreault, K. Chakrabarty, C. -C. Chen, et al. High-Entropy Borides under Extreme Environment of Pressures and Temperatures. *Materials* **2022**, 15, 3239. https://doi.org/10.3390/ma15093239.

[13] M. Duan, I.V. Solodkyi, Y.I. Bogomol, Recent Advancements in the Synthesis of High-Entropy Boride Ceramics: A Review. *J. Superhard Mater.* **2023**, 45, 434–443. https://doi.org/10.3103/S1063457623060023.

[14] S. Filipovic, N. Obradovic, G. E. Hilmas, W. G. Fahrenholtz, D. W. Brenner, et al. A super-hard high entropy boride containing Hf, Mo, Ti, V, and W. *J. Am. Ceram. Soc.* **2024**, 107, 4430-4435. https://doi.org/10.1111/jace.19795.

[15] L. Feng, F. Monteverde, W. G. Fahrenholtz, G. E. Hilmas, Superhard high-entropy AlB_2-type diboride ceramics. *Scr. Mater.* **2021**, 199, 113855. https://doi.org/10.1016/j.scriptamat.2021.113855.

[16] Avcıoğlu, C., Avcıoğlu, S. Transition Metal Borides for All-in-One Radiation Shielding. *Materials* **16**, 6496 (2023). https://doi.org/10.3390/ma16196496.

[17] J. Gild, Y. Zhang, T. Harrington, S. Jiang, T. Hu, et al. High-Entropy Metal Diborides: A New Class of High-Entropy Materials and a New Type of Ultrahigh Temperature Ceramics. *Sci. Rep.* **2016**, 6, 37946. https://doi.org/10.1038/srep37946.

[18] A. B. Peters, D. Zhang, S. Chen, C. Ott, C. Oses, et al. Materials design for hypersonics. *Nat. Commun.* **2024**, 15, 3328. https://doi.org/10.1038/s41467-024-46753-3.

[19] R. Wang, Y. Sun, F. Zhang, F. Zheng, Y. Fang, et al. High-Throughput Screening of Strong Electron–Phonon Couplings in Ternary Metal Diborides. *Inorg. Chem.* **2022**, 61, 18154–18161. https://pubs.acs.org/doi/10.1021/acs.inorgchem.2c02829.

[20] B. Post, F. W. Glaser, D. Moskowitz, Transition metal diborides. *Acta Metall.* **1954**, 2, 20-25. https://doi.org/10.1016/0001-6160(54)90090-5.

[21] Y. Zhang, W. M. Guo, Z. B. Jiang, Q. Q. Zhu, S. K. Sun et al. Dense high-entropy boride ceramics with ultra-high hardness. *Scr. Mater.* **2019**, 164, 135–139. https://doi.org/10.1016/j.scriptamat.2019.01.021.

[22] Y. Zhang, Z. B. Jiang, S. K. Sun, W. M. Guo, Q. S. Chen, et al. Microstructure and mechanical properties of high-entropy borides derived from boro/carbothermal reduction. *J. Eur. Ceram. Soc.* **2019**, 39, 3920–3924. https://doi.org/10.1016/j.jeurceramsoc.2019.05.017.

[23] J. Nie, Y. Zhi, Y. Fan, Y. Zhao, X. Liu, One-step synthesis of high-entropy diborides with hierarchy structure and high hardness via aluminum-melt reaction method. *Mater. Res. Lett.* **2023**, 12, 88–96. https://doi.org/10.1080/21663831.2023.2292079.

[24] J. Gu, J. Zou, S. -K. Sun, H. Wang, S. -Y. Yu, et al. Dense and pure high-entropy metal diboride ceramics sintered from self-synthesized powders via boro/carbothermal reduction approach. *Sci. China Mater.* **2019**, 62, 1898–1909. https://doi.org/10.1007/s40843-019-9469-4.

[25] L. Feng, W. G. Fahrenholtz, G. E. Hilmas, F. Monteverde, Effect of Nb content on the phase composition, densification, microstructure, and mechanical properties of high-entropy boride ceramics. *J. Eur. Ceram. Soc.* **2021**, 41, 92–100. https://doi.org/10.1016/j.jeurceramsoc.2020.08.058.

[26] F. Monteverde, F. Saraga, M. Gaboardi, Compositional disorder and sintering of entropy stabilized (Hf,Nb,Ta,Ti,Zr)B_2 solid solution powders. *J. Eur. Ceram. Soc.* **2020**, 40, 3807–3814. https://doi.org/10.1016/j.jeurceramsoc.2020.04.026.

[27] Y. Zhang, S. -K. Sun, W. Zhang, Y. You, W. -M. Guo, et al. Improved densification and hardness of highentropy diboride ceramics from fine powders synthesized via borothermal reduction process. *Ceram. Int.* **2020**, 46, 14299–14303. https://doi.org/10.1016/j.ceramint.2020.02.214.

[28] G. Tallarita, R. Licheri, S. Garroni, R. Orrù, G. Cao, Novel processing route for the fabrication of bulk high-entropy metal diborides. *Scr. Mater.* **2019**, 158, 100-104. https://doi.org/10.1016/j.scriptamat.2018.08.039.

[29] Y. F. Ye, Q. Wang, J. Lu, C. T. Liu, Y. Yang, High-entropy alloy: challenges and prospects. *Mater. Today* **2016**, 19, 349–362. https://doi.org/10.1016/j.mattod.2015.11.026.

[30] O. N. Senkov, S. V. Senkova, C. Woodward, D. B. Miracle, Low-density, refractory multi-principal element alloys of the Cr-Nb-Ti-V-Zr system: microstructure and phase analysis. *Acta Mater.* **2013**, 61, 1545–1557. https://doi.org/10.1016/j.actamat.2012.11.032.

[31] X. -Q. Chen, H. Niu, D. Li, Y. Li, Modeling hardness of polycrystalline materials and bulk metallic glasses. *Intermetallics* **2011**, 19, 1275–1281 (). https://doi.org/10.1016/j.intermet.2011.03.026.

[32] D.M. Teter, Computational alchemy: the search for new superhard materials. *MRS Bull.* **1998**, 23, 22–27. https://doi.org/10.1557/S0883769400031420.

[33] Y. Tian, B. Xu, Z. Zhao, Microscopic theory of hardness and design of novel superhard crystals. *Int. J. Refract. Met. Hard Mater.* **1998**, 33, 93–106. https://doi.org/10.1016/j.ijrmhm.2012.02.021.

[34] M. Qin, J. Gild, H. Wang, T. Harrington, K. S. Vecchio, et al. Dissolving and stabilizing soft WB_2 and MoB_2 phases into high-entropy borides via boron-metals reactive sintering to attain higher hardness. *J. Eur. Ceram. Soc.* **2020**, 40, 4348-4353. https://doi.org/10.1016/j.jeurceramsoc.2020.03.063.

[35] D. Demirskyi, T. Nishimura, K. Yoshimi, O. Vasylkiv, High-strength, medium entropy Zr-Ta-Nb diboride ceramics. *Scr. Mater.* **2023**, 225, 115170. https://doi.org/10.1016/j.scriptamat.2022.115170.

[36] D. Kalish, E. V. Clougherty, K. Kreder, Strength, Fracture Mode, and Thermal Stress Resistance of HfB_2 and ZrB_2. *J. Am. Ceram. Soc.* **1969**, 52, 30-36. https://doi.org/10.1111/j.1151-2916.1969.tb12655.x.

[37] W. H. Rhodes, E. V. Clougherty, D. Kalish, Research and Development of Refractory Oxidation-Resistant Diborides, Technical Report AFML-TR-68-190 (Preprint) https://apps.dtic.mil/sti/pdfs/AD0839956.pdf submitted: **1970**.

[38] E. W. Neuman, G. E. Hilmas, W. G. Fahrenholtz, Strength of Zirconium Diboride to 2300°C, *J. Am. Ceram. Soc.* **2013**, 96, 47-50. https://doi.org/10.1111/jace.12114.

[39] D. Demirskyi, T. Nishimura, Y. Sakka, O. Vasylkiv, High-strength TiB_2–TaC ceramic composites prepared using reactive spark plasma consolidation, *Ceram. Int.* **2016**, 42, 1298–1306. https://doi.org/10.1016/j.ceramint.2015.09.065.

[40] D. Demirskyi, T. S. Suzuki, K. Yoshimi, O. Vasylkiv, High-temperature reactive synthesis of the Zr–Ta multiboride with a supercomposite structure. *J. Am. Ceram. Soc.* **2022**, 105, 6989-7002. https://doi.org/10.1111/jace.18653.

[41] D. Demirskyi, I. Solodkyi, T. Nishimura, Y. Sakka, O. Vasylkiv, High-temperature strength and plastic deformation behavior of niobium diboride consolidated by spark plasma sintering. *J. Am. Ceram. Soc.* **2017**, 100, 5295–5305. https://doi.org/10.1111/jace.15048.

[42] D. Demirskyi, O. Vasylkiv, Spark plasma sintering and high-temperature strength of B_6O–TaB_2 ceramics. *J. Eur. Ceram. Soc.* **2017**, 37, 3009-3014. https://doi.org/10.1016/j.jeurceramsoc.2017.02.052.

[43] G. de With, High temperature fracture of boron carbide: experiments and simple theoretical models. *J. Mater. Sci.* **1984**, 19, 457–466. https://doi.org/10.1007/BF02403232.

[44] O. Vasylkiv, D. Demirskyi, P. Badica, T. Nishimura, A. I. Y. Tok, et al. Room and high temperature flexural failure of spark plasma sintered boron carbide. Ceram. Int. **2016**, 42, 7001–7013. https://doi.org/10.1016/j.ceramint.2016.01.088.

[45] O. Vasylkiv, D. Demirskyi, H. Borodianska, Y. Sakka, P. Badica, High temperature flexural strength in monolithic boron carbide ceramic obtained from two different raw powders by Spark Plasma Sintering. *J. Ceram. Soc. Jpn.* **2016**, 124, 587–592. https://doi.org/10.2109/jcersj2.15289.

[46] G. E. Neuman, Ultra-high temperature mechanical properties of a zirconium diboride–zirconium carbide ceramic. *J. Am. Ceram. Soc.* **2016**, 99, 597–603. https://doi.org/10.1111/jace.13990.

[47] H. R. Baumgartner, R. A. Steiger, Sintering and properties of titanium diboride made from powder synthesized in a plasma-arc heater. *J. Am. Ceram. Soc.* **1984**, 67, 207–212. https://doi.org/10.1111/j.1151-2916.1984.tb19744.x.

[48] R. A. Adrievskii, Properties of nanocrystalline refractory compounds (review), Powder Metall. Met. Ceram. **1994**, 32, 935–941. https://doi.org/10.1007/BF00559654.

[49] J. S. Haggerty, D. W. Lee, Plastic deformation of ZrB_2 single crystals, *J. Am. Ceram. Soc.* **1971**, 54, 572–576. https://doi.org/10.1111/j.1151-2916.1971.tb12210.x.

[50] I.G. Talmy E.J. Wuchina, J.A. Zaykoski, M.M. Opeka, Properties of ceramics in the NbB_2–CrB_2 system. *Ceram. Eng. Sci. Proc.* **1996**, 3, 128-135. https://doi.org/10.1002/9780470314821.ch15.

[51] D. Demirskyi, Y. Sakka, In situ fabrication of B_4C–NbB_2 eutectic composites by spark-plasma sintering. *J. Am. Ceram. Soc.* **2014**, 97, 2376-2379. https://doi.org/10.1111/jace.13083.

[52] D. Demirskyi, Y. Sakka, Fabrication, microstructure and properties of in situ synthesized B_4C–NbB_2 eutectic composites by spark plasma sintering. *J. Ceram. Soc. Jpn.* **2015**, 123, 33-37. https://doi.org/10.2109/jcersj2.123.33.

[53] D. Demirskyi, O. Vasylkiv, Mechanical properties of SiC–NbB_2 eutectic composites by in situ spark plasma sintering. *Ceram. Int.* **2016**, 42, 19372-19385. https://doi.org/10.1016/j.ceramint.2016.09.110.

[54] D., Demirskyi, O. Vasylkiv, Flexural strength behavior of a ZrB_2–TaB_2 composite consolidated by non-reactive spark plasma sintering at 2300 °C. *Int. J. Refract. Met. Hard Mater.* **2017**, 66, 31–35. https://doi.org/10.1016/j.ijrmhm.2017.02.003.

[55] A. Kuncser, O. Vasylkiv, H. Borodianska, D. Demirskyi, P. Badica, High bending strength at 1800 °C exceeding 1 GPa in TiB_2-B_4C composite. *Sci. Rep.* **2023**, 13, 6915. https://doi.org/10.1038/s41598-023-33135-w.

[56] D. Demirskyi, H. Sepehri-Amin, T. S. Suzuki, K. Yoshimi, O. Vasylkiv, Ultra-high temperature flexure and strain driven amorphization in polycrystalline boron carbide bulks. *Scr. Mater.* **2022**, 210, 114487. https://doi.org/10.1016/j.scriptamat.2021.114487.

[57] S. J. Sitler, K. S. Raja, I. Charit, ZrB_2-HfB_2 solid solutions as electrode materials for hydrogen reaction in acidic and basic solutions. *Mater. Lett.* **2017**, 188, 239-243. https://doi.org/10.1016/j.matlet.2016.10.122.

[58] D. Demirskyi, O. Vasylkiv, Consolidation and grain growth of tantalum diboride during spark plasma sintering. *Ceram. Int.* **2016**, 42, 16396-16400. https://doi.org/10.1016/j.ceramint.2016.07.059.

[59] D. Demirskyi, T. Nishimura, T. S. Suzuki, K. Yoshimi, O. Vasylkiv, Reactive consolidation and high-temperature strength of HfB_2–SiB_6. *J. Eur. Ceram. Soc.* **2022**, 42, 4783-4792. https://doi.org/10.1016/j.jeurceramsoc.2022.05.004.

[60] B. Z. Dacic, V. Jokanovic, B. Jokanovic and M. D. Dramicanin, Thermodynamics of gas phase carbothermic reduction of boron-anhydride. *J. Alloys Compd.* **2006**, 413, 198-205. https://doi.org/10.1016/j.jallcom.2005.03.117.

[61] Japanese Industrial Standard (JIS), High temperature bending strength test method for fine ceramics, *JIS R* **2008**, 1604. https://kikakurui.com/r1/R1604-2008-01.html.

[62] ASTM International, Standard Test Method for Flexural Strength of Advanced Ceramics at Elevated Temperatures, ASTM C1211-13 (upgraded to ASTM C1211-18(2023), *Book of Standards Volume* **2023**, 15.01. https://doi.org/10.1520/C1211-18R23.

[63] ASTM International, Standard Test Methods for Density of Compacted or Sintered Powder Metallurgy (PM) Products Using Archimedes' Principle, ASTM B962-23, *Book of Standards Volume* **2023**, 02.05. https://doi.org/10.1520/B0962-23].

[64] ASTM International, Standard Test Method for Young's Modulus, Tangent Modulus, and Chord Modulus, ASTM E111-04, *Book of Standards Volume* **2017**, 03.01. https://doi.org/10.1520/E0111-17].

[65] J. -X. Liu, X. -Q. Shen, Y. Wu, F. Li, Y. Liang, G. -J. Zhang, Mechanical properties of hot-pressed high-entropy diboride-based ceramics. J. Adv. Ceram. **2020**, 9, 503-510. https://doi.org/10.1007/s40145-020-0383-8.

[66] S. Baik, P. F. Becher, Effect of oxygen contamination on densification of TiB_2. *J. Am. Ceram. Soc.* **1987**, 70, 527–530. https://doi.org/10.1111/j.1151-2916.1987.tb05699.x.

[67] J. Amodeo, S. Merkel, C. Tromas, P. Carrez, S. Korte-Kerzel, et al. Dislocations and Plastic Deformation in MgO Crystals: A Review. *Crystals* **2018**, 8, 240. https://doi.org/10.3390/cryst8060240.

[68] A. Nie, Y. Bu, J. Huang, Y. Shao, Y. Zhang, et al. Direct Observation of Room-Temperature Dislocation Plasticity in Diamond. *Matter* **2020**, 2, 1222-1232. https://doi.org/10.1016/j.matt.2020.02.011.

[69] B. Jiang, G. J. Weng, A theory of compressive yield strength of nano-grained ceramics. *Int. J. Plast.* **2004**, 20, 2007-2026. https://doi.org/10.1016/j.ijplas.2003.10.010.

[70] F. Wang, X. Yan, C. Zhang, L. Deng, Y. Lu, et al. Localized plasticity in silicon carbide ceramics induced by laser shock processing. *Materialia* **2019**, 6, 100265. https://doi.org/10.1016/j.mtla.2019.100265.

[71] C. Shen, J. Li, T. Niu, J. Cho, Z. Shang, et al. Achieving room temperature plasticity in brittle ceramics through elevated temperature preloading. *Sci. Adv.* **2024**, 10, 1-10. https://doi.org/10.1126/sciadv.adj4079.

[72] F. Östlund, K. Rzepiejewska-Malyska, K. Leifer, L. M. Hale, Y. Tang, et al. Brittle-to-Ductile Transition in Uniaxial Compression of Silicon Pillars at Room Temperature. *Adv. Funct. Mater.* **2009**, 19, 2439–2444. https://doi.org/10.1002/adfm.200900418.

[73] J. Michler, K. Wasmer, S. Meier, F. Östlund, K. Leifer, Plastic deformation of gallium arsenide micropillars under uniaxial compression at room temperature. *Appl. Phys. Lett.* **2007**, 90, 043123. https://doi.org/10.1063/1.2432277.

[74] S. Kiani, C. Ratsch, A.M. Minor, S. Kodambaka, J.-M. Yang, Orientation- and size-dependent room-temperature plasticity in ZrC crystals. *Phil. Mag.* **2015**, 95, 985-997. https://doi.org/10.1080/14786435.2015.1012568.

[75] H. Xia, B. Wang, Z. Zhang, 4.01 - Mechanics of Microstructured Composites. *Comprehensive Mechanics of Materials* **2024**, *4* (ed. Silberschmidt, V.), 1-21. https://doi.org/10.1016/B978-0-323-90646-3.00054-X.

[76] F. Ling, K. Luo, L. Hao, Y. Gao, Z. Yuan, Q. Gao, Y. Zhang, Z. Zhao, J. He, D. Yu, Universal Phase Transitions of AlB_2-Type Transition-Metal Diborides. *ACS Omega* **2020**, 5, 4620-4625. https://doi.org/10.1021/acsomega.9b04260.

[77] E. Fendler, O. Babushkin, T. Lindbäck, R. Telle, G. Petzow, Thermal Expansion of Diboride Solid Solutions. In: Carlsson, R., Johansson, T., Kahlman, L. (eds) *4th International Symposium on Ceramic Materials and Components for Engines* **1992**, Springer, Dordrecht. https://doi.org/10.1007/978-94-011-2882-7_16.

Copyright License - Fig 1c

Copyright License - Fig 1c

Copyright License - Fig 1c

Table of Contents (ToC)

High-Entropy Ti, Zr, Hf, Ta Multiphase Diboride with Deformation Resistance up to 2000 °C

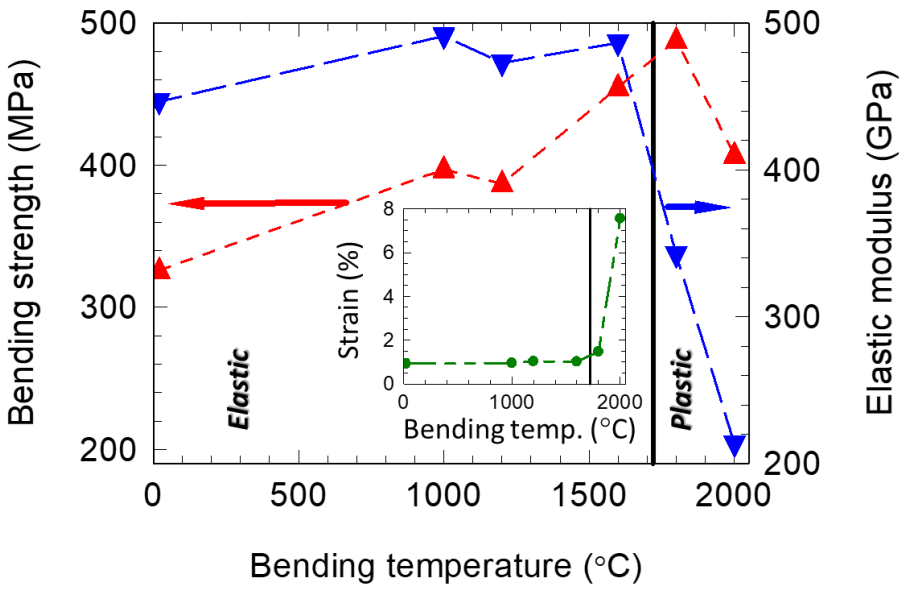

Ceramics are brittle and strength decreases with temperature. The multiphase high-entropy $(Ti_{0.25}Ta_{0.25}Hf_{0.25}Zr_{0.25})B_2$ with heterogeneity at the nano- and microscale demonstrates deformation resistance up to 2000 °C, with maximum bending strength at 1800 °C. At 2000 °C, it exhibits a substantial plastic deformation, resulting in a strain of 7.5%, and maintains a bending strength 25% higher than that at room temperature.